Coercivity-driven surface acoustic wave induced ferromagnetic resonance

Ashwin Kavilen Vythelingum, Timothée Tremblais, Doan Nguyen Ba, Djoudi Ourdani, Erwan Dandeu, Catherine Gourdon, Vincent Laude, L. Thevenard

Coercivity-driven surface acoustic wave induced ferromagnetic resonance

A. K. Vythelingum,[†] T. Tremblais,[†] D. Nguyen,[†] D. Ourdani,[†] E. Dandeu,[†] V. Laude,[‡] C. Gourdon,[†] and L. Thevenard[*,†]

[†]*Sorbonne Université, CNRS, Institut des Nanosciences de Paris, INSP, F-75005 Paris, France*

[‡]*Université Marie et Louis Pasteur, CNRS, Institut FEMTO-ST, F-25000 Besançon, France*

E-mail: thevenard@insp.jussieu.fr

Abstract

We report the observation of surface acoustic wave (SAW)-driven ferromagnetic resonance (FMR) on polycrystalline FeRh in its ferromagnetic phase. A strong hysteresis of the magnetic fields at resonance is observed and is found to correlate with the static coercivity of the sample, as confirmed by temperature-dependent measurements. The angular dependence of SAW-FMR is furthermore measured and found to exhibit a wide variety of shapes that differ from commonly observed resonance curves. By modeling the hysteresis of the sample using a simple macrospin approach, we show that the observed features result from the softening of the magnetic eigenfrequency and of the magnetoelastic field allowed by hysteresis. This observation opens up the possibility of coupling resonantly SAWs to magnetization dynamics for both low magnetic fields and low frequencies, which is normally possible only for samples presenting magnetic anisotropy. Long considered a problem to be reckoned with, hysteresis may

now instead offer an appealing alternative for on-chip integration of magnetic SAW sensors.

Keywords

Ferromagnetic resonance, Surface acoustic wave, Magneto-acoustic coupling

1 Introduction

Great progress has been achieved over the past decade in understanding how spin waves or magnons interact with bulk and surface acoustic waves (SAWs) via magnetoelasticity.[1] Since magnetic properties finely depend on interatomic distances, strain waves are an interesting nonthermal and tunable lever to manipulate a magnetic system, especially when they resonate with magnetic eigenfrequencies. Experiments involving piezoelectrically excited SAW are typically performed on metallic, semiconducting, or insulating ferromagnets such as nickel, cobalt or Fe_3Si,[2–6] GaMnAs,[7] or YIG,[8] as well as synthetic 2D ferro- and antiferromagnets.[9–11] Special attention has been paid to the very general features of this interaction, in particular the influence of SAW frequency and power, the magnetic anisotropy of the layer, and the direction of the applied magnetic field.

Paralleling such developments in the ferromagnetic resonance community, the magnetic field sensing community has developed devices, models, and systems that rely on the same physics but approach questions from an acoustic perspective.[12–17] Measurement of the variations of elastic wave properties with the magnetic field, even very far from magnetic resonance, has indeed proven to offer an interesting alternative to traditional field sensors that are based on magnetoresistance or the Hall effect, with the potential advantage of wireless operation.

Whether using magnetoelasticity to manipulate magnetization or to perform on-chip field measurements via acoustic properties, magnetic hysteresis is at best avoided and at worst

constitutes a real problem to deal with. Magnetic hysteresis appears when SAW attenuation or velocity is measured while the magnetic field is swept along an easy magnetic axis.[3,4,14,18] It is rarely taken into account when modeling the magnetoacoustic interaction.

In this work, we show that coercivity is in fact an alternative way to reach the SAW-driven ferromagnetic resonance (SAW-FMR) regime, allowing resonance at much lower fields and over a much wider range of field angles than when only exploiting the case of (quasi) positively aligned magnetization and magnetic field. For this purpose, we chose an atypical material, FeRh, because of its easily tunable coercivity. This equiatomic alloy exhibits a first-order transition from a ferromagnetic (FM) to an antiferromagnetic (AFM) phase upon cooling. The reduction in FM domain nucleation sites during the transition results in a significant increase in coercivity with decreasing temperature, whereas the remaining magnetic parameters vary much less. We make use of this property to assess the effect of coercivity on SAW-FMR, only focusing on the resonance of the FM fraction of the sample. We then develop a simple model to describe SAW-FMR taking hysteresis into account. Assuming relatively conservative hypotheses such as macrospin rotation, we reproduce the main observed experimental features, such as the dependence with the SAW frequency, the applied temperature, and the field angle.

2 Experimental section

The considered magnetic system consists of a FeRh(h=270 nm) / Ta(100 nm) mesa on a GaAs(001) substrate, over which interdigitated transducers (IDTs) are directly thermally evaporated, as shown in Fig. 1(a) (see Supplemental Information (SI) section A for details on sample fabrication). IDTs are composed of pairs of 4:4 equipotential digits ensuring the excitation of surface acoustic waves of frequency $f = n\dfrac{V_{r,0}}{\lambda_0}$, with $\lambda_0 = 9.5$ μm, $n = 1, 3$, and where $V_{R,0}(T)$ is the temperature-dependent Rayleigh velocity of GaAs.

Magnetization is measured versus temperature on an unpatterned sample grown in the

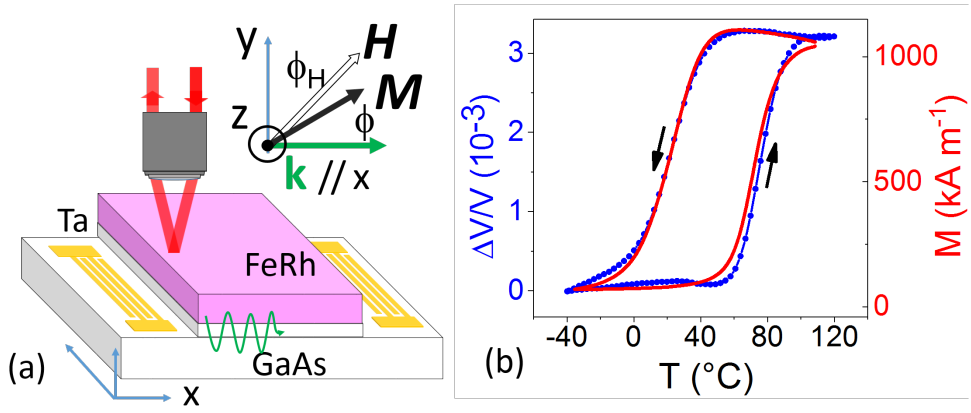

Figure 1: Schematics of the experimental setup. (a) Magnetic properties of the FeRh/Ta/GaAs sample (not to scale, simplified IDT design, see text for details) are measured using longitudinal Kerr microscopy. SAWs are excited and received by IDTs along a $\langle 110 \rangle$ direction of the GaAs substrate. (b) Magnetization measured by SQUID magnetometry is shown versus temperature (red line) for a sample grown in the same batch and is overlaid with the relative acoustic phase velocity variations (f=299 MHz, blue line and symbols, no field applied). The negative slope caused by the decrease of acoustic velocity with temperature was removed and the value at T_{ref} = -40°C was taken as a reference.

same batch (red curve in Fig. 1(b)). A broad AFM to FM transition is apparent, with the magnetization M dropping to 71 kA m^{-1} at -40°C. The patterned sample is then glued onto a chip, micro-bonded, and placed in a variable-temperature cryostat regulated by a continuous flow of liquid nitrogen and a heating resistance.

At $T = 130$°C, for which the sample is in a uniform FM phase, surface acoustic waves are excited at f=299 and 889 MHz in 300-ns-long bursts every 10 μs. After propagation across the delay line (width of the FeRh mesa L=3.4mm, inter-IDT separation L^*=3.547 mm, transit time $\tau(f)$), they are detected by the facing IDT using an oscilloscope, thanks to which the acoustic echo and the electromagnetic parts of the signal can be clearly separated.[7,19] The arrival time of the echo gives an estimate of the group velocity at the corresponding frequency. It matches well with values calculated using the elastic constants of FeRh, Ta and GaAs (see numerical details in SI section B). The centermost part of the acoustic echo is fitted with function $A \sin(2\pi f t + \psi)$, from which the relative SAW amplitude and phase velocity variations are computed from relations $\Delta\Gamma(H,T) = \frac{20}{L} \log\left(\frac{A(H,T)}{A(H_{\mathrm{ref}},T)}\right)$ and

$\frac{\Delta V}{V}(H,T)=\frac{\psi(H,T)-\psi(H_{\rm ref},T_{\rm ref})}{2\pi f\tau(f)}$, respectively.

We first measure the SAW phase velocity without applied field versus temperature, starting from -40°C. As expected for acoustic waves, a steady decrease of the phase velocity is observed with temperature, on top of which appears a clear hysteretic behavior, resulting from the presence of the FeRh layer. Once this negative slope has been removed, a clear opening appears (blue curve in Fig. 1(b)), due to the significantly different elastic constants of FeRh in the AFM and FM phases.[20] The SAW phase velocity variations with temperature match perfectly those of magnetization (red curve in Fig. 1(b)). Those variations are thus an excellent indication of the ferromagnetic fraction explored by surface acoustic waves. This fraction, that will be labeled $x_{\rm FM}$ in the following, varies between 0 (AFM phase) and 1 (FM phase).

3 Results and discussion

3.1 Field parallel to the SAW wavevector

We first conduct SAW-FMR experiments in the uniform FM phase at $T = 130$°C. The SAW amplitude and phase velocity are monitored as the magnetic field is swept from $\mu_0 H_{\rm ref} = 200$ to -200 mT and back, and are normalized to their value at saturation. Judging from hysteresis cycles obtained for a very similar sample,[21] this field is sufficient to saturate the magnetization in the uniform FM phase. The field is first applied parallel to the SAW wavevector ($\phi_H = 0°$ in the reference frame of Fig. 1(a)). Decreasing the field from positive saturation, Fig. 2 shows that both SAW phase velocity and amplitude first slowly decrease. As the field overshoots zero, a clear hysteretic behavior appears. For $f = 299$ MHz, both amplitude and velocity variations drop around $|\mu_0 H_{\rm max}| = 3.2 \pm 0.1$ mT down to about $-1.3\,{\rm dB\,cm^{-1}}$ and $-2.9\,10^{-4}$, respectively. For $f = 889$ MHz a similar behavior is observed, with the maximum amplitude variations reaching -38 $\rm dB\,cm^{-1}$ at about 2.7 ± 0.1 mT, whereas the maximum velocity variations only double to $-4.5\ 10^{-4}$. Similar hysteretic signals under

SAW excitation have been observed before on nickel, FeGa, and FeCoSiB, with the field giving the position (respectively depth) of the maximum attenuation varying weakly (respectively strongly) with SAW frequency.[3,4,14,18,22,23] In-depth modeling, however, has not yet been proposed. We demonstrate in the following that the observation we make is indeed SAW-driven FMR, and anticipate this interpretation by renaming fields at the maximum attenuation/velocity variations as "resonance fields" $H_{\rm res}$.

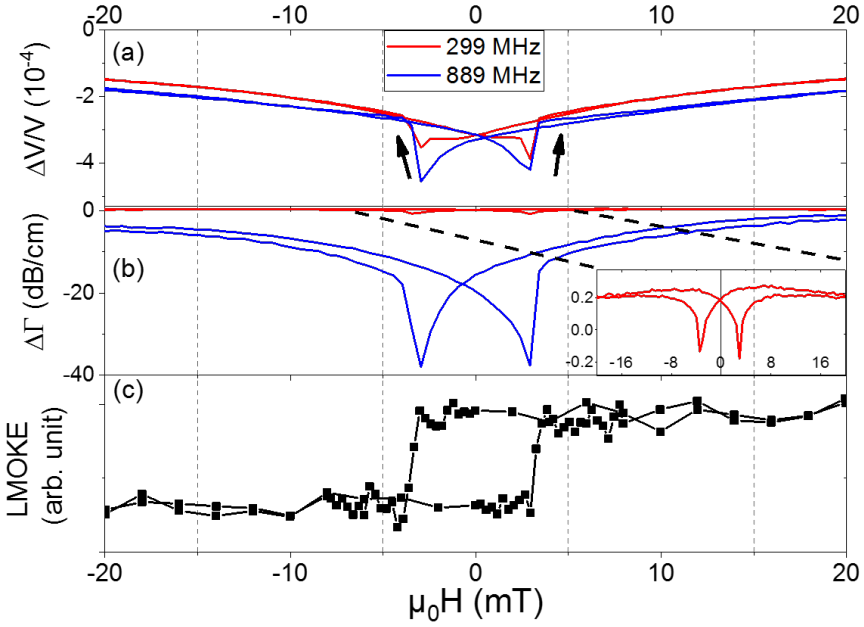

Figure 2: SAW-FMR experiment at T=130°C, with the field applied along the SAW wavevector for f=299 and 889 MHz. SAW phase velocity (a) and amplitude (b) variations are shown versus applied field. The inset in (b) is a zoom on the 299 MHz curve. (c) Longitudinal Kerr cycle obtained by averaging a microscopy image of the FeRh mesa taken in front of the exciting IDT.

In order to relate acoustic data with the static magnetic behavior, we then record a longitudinal Kerr microscopy (LMOKE) hysteresis cycle in front of the excitation transducer[1]. The hysteresis cycle is relatively square, with coercitive field $\mu_0 H_c = 3.3$ mT (Fig. 2(c)), and aligns with the resonance fields seen in the SAW-FMR data. Magnetization goes from

[1] A linearly polarized 635 nm LED source is focused in the back focal plane of a 0.4 NA objective. Reflected light is detected through a partially crossed analyzer and measures the projection of the magnetization along the SAW direction. Averaging the signal over the 220 × 240 μm^2 FeRh area, the hysteresis cycle can be reconstituted.

positive to negative saturation over a range of about 1 mT, with data points in the switching step indicating the presence of multiple domains.

Systematic SAW-FMR experiments are then performed following an identical procedure, decreasing temperature from the fully uniform phase at $T = 130°C$ until the signal is dominated by noise, around $T = 20°C$ (Fig. 3(a)). The signal maintains a similar shape but decreases in amplitude, as expected from the decreasing FM fraction of the layer.[24] The resonance fields for f=299 and 889 MHz are then plotted versus temperature, along with the coercivity measured as detailed above (Fig. 3(b)). The resonance field for f= 889 MHz is systematically fractions of mT lower than for f= 299 MHz. Both closely follow coercivity at all temperatures. Coercivity diverges from its high temperature value as the ferromagnetic fraction decreases from 1 (dashed orange line in Fig. 3(b)).

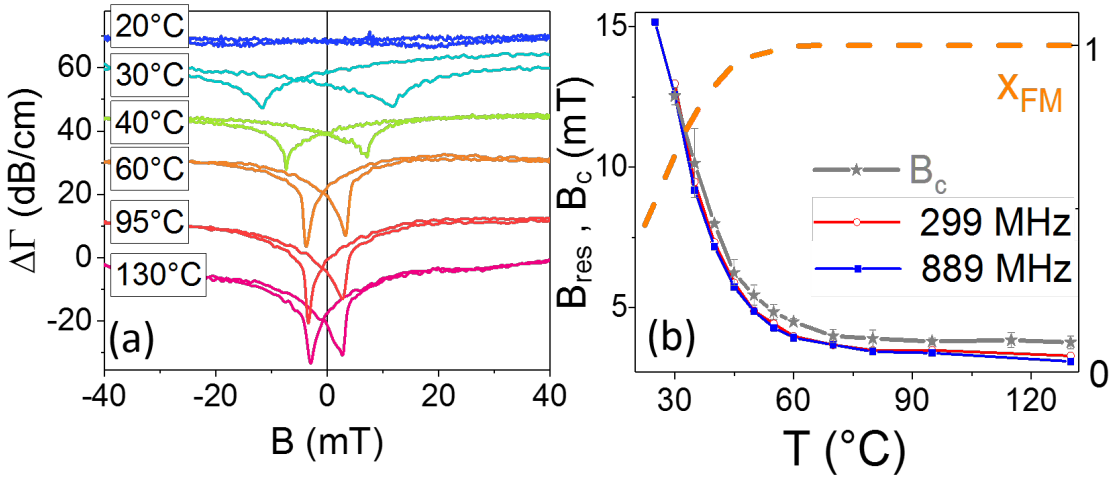

Figure 3: (a) Relative amplitude variations (offset for clarity) at varying temperature for f=889 MHz and applied field parallel to $\boldsymbol{k}$ (ϕ_H=0°). See SI section E for velocity variations at f=889 MHz and data for f=299 MHz. (b) Resonance fields obtained from amplitude variations for f=299 and 889 MHz are overlaid with the coercive field measured by LMOKE microscopy. The dashed orange line is the FM fraction deduced from the relative velocity measurement (see Fig. 1(b)).

3.2 Angular dependence of SAW-FMR

Having identified that the resonance field matches the coercivity when **H** is parallel to **k**, we now perform SAW-FMR at varying field angles, in order to probe the dependence of the effective magneto-elastic field with the magnetization direction. In particular, if the magnetization is strictly in-plane and follows the field direction, no torque is expected when **H** is perpendicular to the wave-vector **k** of a Rayleigh wave.[3,25,26]

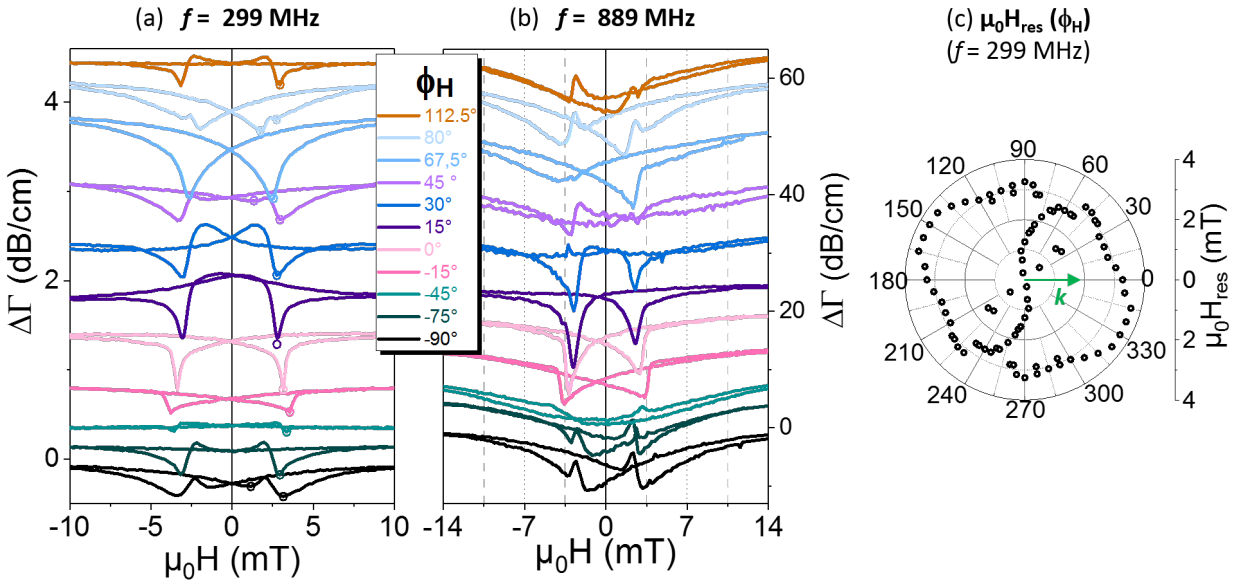

Figure 4: SAW-FMR at selected field angles (see the animations in the SI for the other angles) for (a) f=299 MHz and (b) f=889 MHz. (c) The resonance field $H_{\rm res}$ for f=299 MHz (open circle symbols in panel (a)) is shown as a function of the field angle ϕ_H. ϕ_H is counted with respect to the SAW wavevector direction (shown with the green arrow).

The field angle is varied between $\phi_H = -90°$ and $+120°$ in steps of 7.5°, for both frequencies. Since the hysteresis cycles cover both positive and negative $(\phi_H + \pi)$ fields, this setting conveniently provides partial redundancy in the data. A selection of amplitude curves is presented in Fig. 4(a,b) (other field angles and SAW phase velocity data are provided in SI section E and animations). Strikingly, hysteresis persists at all angles and resonance never disappears. Resonance is the shallowest around $\phi_H = -45°$ and the deepest around $\phi_H = 67°$. Its shape also varies from that of a single Lorentzian dip at $\phi_H = 0°$ to a double

dip, *e.g.* at $\phi_H = 80-90°$, or a Lorentzian-derivative-like shape, *e.g.* at $\phi_H = 22°$, 30°. This variable shape makes it difficult to pinpoint a single resonance field, so we tentatively select the local minima indicated with open symbols in Fig. 4(a). We then plot the resonance field versus field angle in Fig. 4(c). The envelope of the polar plot varies between 2.5 and 3.6 mT and exhibits slight uniaxial anisotropy along $\approx -(10-15)°$. For $f = 299$ MHz a weak non-reciprocity appears, since $\Delta\Gamma(+H_{res}) \neq \Delta\Gamma(-H_{res})$ and $\frac{\Delta V}{V}(+H_{res}) \neq \frac{\Delta V}{V}(-H_{res})$. For $f = 889$ MHz, non-reciprocity is extremely marked and completely distorts the "double-dip" lines. Changing the field angle to $\phi_H = -90°$ confirms the sign of the non-reciprocity (full and dashed lines in Fig. 6(d)). We show later that most features of the SAW-FMR data can be qualitatively explained by modeling the system as a hysteretic macrospin system.

4 SAW-FMR model

4.1 Overview of the SAW-FMR model

In a SAW-FMR transmission experiment, an acoustic wave propagates across a magnetic layer that is usually much thinner than the wavelength. The amplitude and velocity of the SAW is modified through the dynamic interaction of strain and magnetization. Along the past decade, various reports have demonstrated for various ferromagnetic and even antiferromagnetic systems that this effect can be modeled using a simple FMR-like approach.[3,9,25,27,28] Specifically, the magnetization dynamic equation is solved with magnetoelastic coupling introduced in the form of an effective field $\boldsymbol{b}_{\rm me}$ oscillating at frequency f. The effective field is derived from the magnetoelastic energy E_{me} as $\boldsymbol{b}_{\rm me} = -\nabla_{\boldsymbol{M}} E_{\rm me}$. Very much like the rf field in a coplanar waveguide, it forces magnetization precession. The problem is then treated from a magnetic point of view by equating the power gained by the magnetic system, $\Delta P_{\rm mag}$, with the power lost by the acoustic system, $\Delta P_{\rm ac}$ (see Eq. 1). Variations of the acoustic power are then expressed as a function of those of the acoustic wavevector using a first order

expansion[3]

$$\Delta P_{\mathrm{ac}} = -2\,\Delta k\,L\,P_{\mathrm{ac},0} = \Delta P_{\mathrm{mag}}, \tag{1}$$

$$\text{with} \quad P_{\mathrm{ac},0} = \frac{1}{2}\,W\,\rho\,V_R\,\omega^2 \int\limits_{\mathrm{FeRh}} |u_i(z)|^2 dz. \tag{2}$$

In this expression, $P_{\mathrm{ac},0}$ is the acoustic power within the magnetic layer before traveling across the delay line,[29] ρ is the mass density of FeRh, W the width of the IDT or acoustic aperture, and u_i are the components of displacements. $P_{\mathrm{ac},0}$ is calculated explicitly for each frequency by solving the elastic propagation equation in the FeRh/Ta/GaAs stack (see details and numerical values in SI section B). ΔP_{mag} is the magnetic power acquired by the layer. It depends on the magnetoelastic field (explicited in the following section) and on the susceptibility χ (in Tesla units, see SI section C). Note that the latter peaks at the magnetic eigenfrequency, *i.e.* for $f_0(H) = f$. The expression for ΔP_{mag} is

$$\Delta P_{\mathrm{mag}} = -i\omega\frac{M_s}{2} \int\limits_{V_{mag}} \boldsymbol{b}^*_{\mathrm{me}} \cdot [\chi]\,\boldsymbol{b}_{\mathrm{me}} dV. \tag{3}$$

Finally, the SAW amplitude and phase velocity variations are computed with respect to a reference state (H_{ref}) from the dissipative/dispersive components of the complex wavevector variations Δk

$$\begin{cases} \Delta\Gamma &= \dfrac{20}{L}\log\left[\exp(L\left[-\Im(\Delta k) + \Im(\Delta k_{\mathrm{ref}})\right])\right], \\ \dfrac{\Delta V}{V} &= -\dfrac{\Re\left[\Delta k\right] - \Re\left[\Delta k_{\mathrm{ref}}\right]}{k}. \end{cases} \tag{4}$$

4.2 Magnetoacoustic interaction

FeRh is known for its strong volume magnetostriction across the phase transition.[30,31] It has indeed been recently exploited to shift the transition of FeRh by a few degrees using surface acoustic waves.[32] There is however very little information on its Joule magnetostriction,[31]

which here will be assumed to yield a magneto-elastic energy of the form:[33,34]

$$E_{\mathrm{me}} = B_s \left(\varepsilon_{xx} m_x^2 + \varepsilon_{zz} m_z^2\right) + 2(B_s \varepsilon_{xz} + K_{\mathrm{eff}} \omega_{zx}) m_x m_z. \tag{5}$$

In this expression, $m_i = \dfrac{M_i}{M_s}$ are the reduced magnetization components and ε_{xz}, ε_{xx}, ε_{zz} and ω_{zx} are the strain and rotation components of the Rayleigh wave traveling along x. B_s (in $\mathrm{J\,m^{-3}}$ units) is an isotropic magnetoelastic constant. K_{eff} encompasses all out-of-plane anisotropy terms of the form $-K_{\mathrm{eff}} m_z^2$, such as out-of-plane uniaxial anisotropy and shape anisotropy[2] $K_{\mathrm{eff}} = K_\perp - \dfrac{\mu_0 M_s^2}{2}$. The two components of the magneto-elastic effective field, $b_\theta(z,x,t) = -\dfrac{1}{M_s}\dfrac{\partial E_{\mathrm{me}}}{\partial \theta}$, and $b_\phi(z,x,t) = -\dfrac{1}{M_s \sin\theta_{\mathrm{eq}}}\dfrac{\partial E_{\mathrm{me}}}{\partial \phi}$, are perpendicular to the static position of the magnetization given by $(\theta_{\mathrm{eq}}, \phi_{\mathrm{eq}})$ (the full expression is given in SI section D). For the particular case of $\theta_{\mathrm{eq}} = \pi/2$ (in-plane magnetization)

$$\begin{cases} b_\theta(x,t) &= -2\left(\dfrac{B_s}{M_s}\varepsilon_{xz} + \dfrac{K_{\mathrm{eff}}}{M_s}\omega_{zx}\right)\cos\phi_{\mathrm{eq}}\,\exp(i\,(kx-\omega t)), \\ b_\phi(x,t) &= \dfrac{B_s}{M_s}\varepsilon_{xx}\sin(2\phi_{\mathrm{eq}})\,\exp(i\,(kx-\omega t)). \end{cases} \tag{6}$$

The magnetoacoustic interaction is here treated in the linear regime, so that the amplitude and velocity variations should not vary with incoming rf power, as verified experimentally. The model reflects this linearity. Strain amplitudes appearing in $\mathbf{b}_{\mathrm{me}}$ and the acoustic power in the layer $P_{\mathrm{ac},0}$ are both calculated from displacements u_i (Eq. 2). The depth of the resonance depends finely on the frequency-dependent *weights* of the different strain components, and in particular on the longitudinal strain ε_{xx} compared with shear strains ε_{xz} and ω_{xz}. We calculate and average their values over the FeRh layer. We observe in particular that the relative weight of shear strains increases with the SAW frequency (see Table 1 in SI section B).

[2]See the particularly relevant discussion and mathematical proof by Yamamoto *et al.*[35] on why and up to what extent it is legitimate to consider the *static* shape anisotropy term $\dfrac{\mu_0 M_s^2}{2}$ as a prefactor in the magneto-rotation energy.

4.3 Modeling hysteretic SAW-FMR: case study for $\boldsymbol{M} \parallel \boldsymbol{k}$

In order to discuss the $\phi_H = 0°$ data using simple analytical formulae, we need a simple model of the hysteretic behavior. Although the dimensions of the FeRh mesa allow for the existence of a complex domain structure at coercivity (Fig. 2(c)), we make the strong approximation of a domain-free Stoner-Wohlfarth macrospin system, and show that it describes correctly the main features of the data. The energy of the system is assumed to be simply

$$E_0 = -\mu_0 \boldsymbol{M} \cdot \boldsymbol{H} - K_u \cos^2(\phi - \phi_u) \sin^2\theta + \frac{\mu_0 M_s^2}{2} \cos^2\theta. \tag{7}$$

Angles θ and ϕ are defined with respect to the sample normal z and to the SAW wavevector, respectively (Fig. 1(a)). Because the data appear to evidence uniaxial anisotropy close to the x axis (Fig. 4(c)), we will moreover assume $\phi_u = 0°$ in this section, but small deviations around this axis would not change the following derivation. The $\phi_{\mathrm{eq}}(H)$ hysteresis cycle is first calculated (Fig. 5(a)). As expected when the field is applied along an easy axis ($\phi_H = \phi_u$) a sharp switching step is obtained for $\mu_0 H_c = \pm \dfrac{2K_u}{M_s}$.

Assuming a fully in-plane magnetization ($\theta_{\mathrm{eq}} = \pi/2$) , the angular eigenfrequency $\omega_0(H) = 2\pi f_0$ (the full expression is given in SI section C) then simply reads

$$\begin{aligned} \omega_0(H) \;=\; & \frac{\gamma}{M_s(1+\alpha^2)} \sqrt{2K_u \cos 2\phi_{\mathrm{eq}} + \mu_0 H M_s \cos\phi_{\mathrm{eq}}} \\ & \times \sqrt{\mu_0 H M_s \cos\phi_{\mathrm{eq}} + 2K_u \cos^2\phi_{\mathrm{eq}} + \mu_0 M_s^2 \left(1 - P_{00}(k)\right)} \quad , \end{aligned} \tag{8}$$

where γ is the gyromagnetic ratio, α accounts for damping, and $P_{00}(k) = 1-(1-\exp(-kh))/kh$ (see SI sections B and C for numerical values of these parameters). The eigenfrequency varies weakly with the SAW wavevector (red and blue curves in Fig. 5(b)). A clear hysteresis appears in the eigenfrequency between fields $\pm\mu_0 H_c = \pm \dfrac{2K_u}{M_s}$, as compared to the case where the magnetization is always collinear to the field (thick gray line in Fig. 5(b)). Allowing **H** and **M** to be anti-aligned moreover induces a strong softening of the eigenfrequency when

$H = H_c$. Eq. (8) shows that this is due to the canceling of the first square root term at this field. Note that a similar conclusion had been reached to explain out-of-resonance dynamic ΔE measurements performed on FeCoSiB with Love waves.[14] The same phenomenon would also occur were we to choose a cubic anisotropy along x, or even a depinning term of the form $-K_{\rm dep}\cos(\phi_H - \phi_{\rm eq})^2$, as long as there is a field range over which **H** and **M** are anti-parallel (*e.g.* $\phi_{\rm eq} = \pi$ when $H > 0$). Eigenfrequency softening is very convenient to couple SAWs of arbitrary low frequency to magnetic systems whose eigenfrequencies are normally beyond typical SAW frequencies (up to 2-3 GHz).

When magnetization is completely in-plane and along x, the magneto-elastic field has only one non-zero component of amplitude $b_{\theta,0} = 2\left(\frac{B_s}{M_s}\langle|\varepsilon_{xz}|\rangle + \frac{K_{\rm eff}}{M_s}\langle|\omega_{zx}|\rangle\right)\cos\phi_{\rm eq}$, with $\phi_{eq} = 0$ [π]. The magnetic power is simply $\Delta P_{\rm mag} = -i\frac{\omega M_s}{2}V_{\rm mag}|b_{\theta,0}|^2\chi_{11}$, with χ_{11} the first diagonal component of the susceptibility tensor (see SI section C). The SAW amplitude and phase velocity relative variations can now be calculated using Eqs. (1-4) by injecting the field-dependence of $b_{\theta,0}(\phi_{\rm eq})$ and $\chi_{11}(\phi_{\rm eq})$, and the numerical values for the average strain and reference acoustic power $P_{\rm ac,0}$ (Table I of SI). They are plotted for the two frequencies in Fig. 5(c,d). They evidence the same hysteresis as the eigenfrequency (Fig. 5(b)), with a dip at the magnetic field for which f_0 intersects the SAW frequency. The resonance field is thus slightly lower for 889 MHz compared to 299 MHz (see the vertical red and blue arrows in Fig. 5(d)), as also observed experimentally (see comments on the temperature-dependence of $B_{\rm res}$, Fig. 3).

The depth of the resonance is 0.25×10^{-4} (resp., 0.8×10^{-4}) for the phase velocity and -0.8 dB cm^{-1} (resp., -10 dB cm^{-1}) for the amplitude at f=299 MHz (resp., at 889 MHz). This agrees qualitatively with experimental observations of a global increase of amplitude with SAW frequency, but a weaker dependence for velocity variations. The model, however, underestimates both SAW velocity variations and high frequency amplitude variations. A better adjustment could be obtained, *e.g.* by introducing a somewhat artificial proportionality constant between $\Delta P_{\rm mag}$ and $\Delta P_{\rm ac}$ as done by previous authors,[3,27] or by increasing

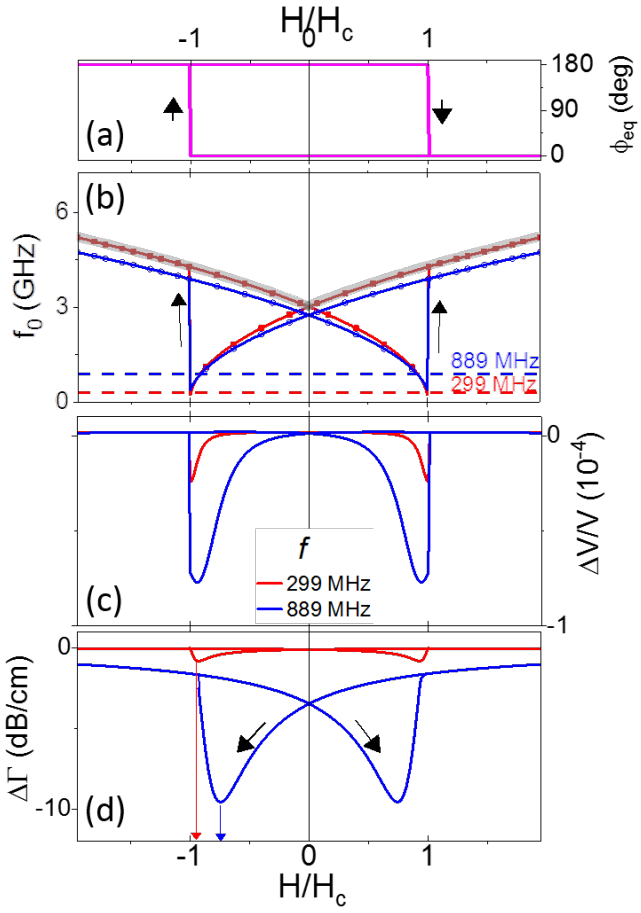

Figure 5: Simplified model in case the magnetic field is aligned with $\boldsymbol{k}$: uniaxial anisotropy is along $\phi_u = 0°$ and there is no depinning term. (a) The hysteresis cycle is plotted as a function of the field normalized to the coercive field $\mu_0 H_c = \dfrac{2K_u}{M_s}$. (b) The spin wave eigenfrequency f_0 is calculated with Eq. (8) assuming hysteresis, for k=0.69 μm^{-1} (f=299 MHz, red line) and k=2.27 μm^{-1} (f=889 MHz, blue line). The thick gray line is the calculation for k=0.69 μm^{-1} assuming no hysteresis. The acoustic wave frequencies f=299 or 889 MHz are indicated by the red and blue dashed horizontal lines, respectively. (c, d) Relative SAW amplitude and velocity variations calculated using Eqs. (3,4) for f=299 and 889 MHz, assuming B_s=5 MJ m^{-3}. Vertical arrows in (d) point to the resonance fields, that are slightly lower at higher frequency.

the magnetoelastic constant. This will be discussed further on.

4.4 Modeling angular SAW-FMR

Analysis of the $\phi_H = 0°$ data has shown that a hysteresis of the equilibrium angle is responsible for hysteretic SAW-FMR. Measurement of the magnetic hysteresis of the FeRh layer at varying field angles in its FM phase would have then allowed us to calculate the corresponding variations $\Delta\Gamma(H, \phi_H)$ and $\Delta V/V(H, \phi_H)$. Unfortunately this type of characterization was not possible due to the joint requirements of high temperature operation (130°C) and application of an in-plane rotating field. Instead, hysteresis was modeled phenomenologically using a combination of various energy terms in order to reproduce the observed angular dependency (Fig. 4). Keeping in mind that (i) hysteresis is needed at all angles and that (ii) a weak uniaxial anisotropy seems to exist slightly off the SAW axis (see Fig. 4(c) for instance), the following energy form was assumed

$$\begin{aligned} E &= -\mu_0 \boldsymbol{M} \cdot \boldsymbol{H} + \frac{\mu_0 M_s^2}{2} \cos^2\theta - K_u \cos^2(\phi - \phi_u) \sin^2\theta \\ &\quad - K_{\text{dep}} \cos^2(\phi - \phi_H) \sin^2(\phi_H - \phi_u) \sin^2\theta \end{aligned} \tag{9}$$

The additional K_{dep} depinning term leads on its own to a sharp switching at $\mu_0 H_{\text{dep}} = \pm\frac{2K_{\text{dep}}}{M_s}$ at all field angles. It is multiplied by $\sin^2(\phi_H - \phi_u)$ in order to come into play only at field angles *away* from ϕ_u. Indeed, in the absence of any term other than K_u, the hysteresis cycle would completely close for $\phi_H = \phi_u + \pi/2$, with magnetization saturating along the hard axis at $\pm\frac{2K_u}{M_s}$.

For each field angle, the following procedure was implemented:(i) the $\phi_{\text{eq}}(H)$ cycle was computed numerically by searching for a local minimum of the total energy; (ii) the magnetoelastic fields and magnetic eigenfrequency were computed; (iii) $\Delta\Gamma(H)$ and $\Delta V/V(H)$ were computed. Using the unique set of parameters $K_u = 4700\,\text{J}\,\text{m}^{-3}$, $K_{\text{dep}} = 3200\,\text{J}\,\text{m}^{-3}$, ϕ_u=-6° and B_s=5 $\text{MJ}\,\text{m}^{-3}$ reproduces qualitatively the shapes observed experimentally. Some dis-

crepancies persist in the exact position of the resonance fields and the depth of the resonance, which are likely due to the strong hypotheses of the model, and will be discussed further. A selection of the calculated amplitude variations is shown in Fig. 6.

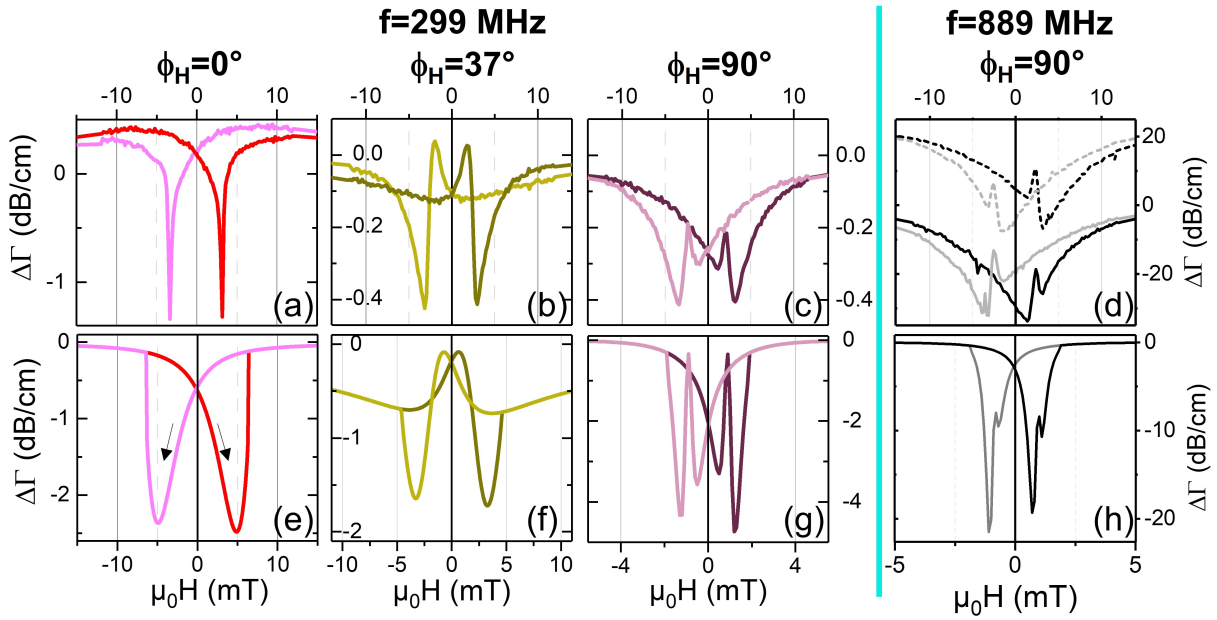

Figure 6: Field angle dependence of SAW FMR. Data in the top row and corresponding modeled curves in the bottom row are calculated using the energy form of Eq. (9) with K_u = 4700 J m^{-3}, $K_{\rm dep}$ = 3200 J m^{-3}, ϕ_u = -6°, and B_s=5 MJm^{-3}. Different shades on a given graph correspond to the up and down field-sweep branches. Selected angles for f = 299 MHz are (a,e) ϕ_H = 0°, (b,f) ϕ_H = 37°, and (c,g) ϕ_H = ±90°. Selected angles for f=889 MHz are (d,h) ϕ_H = 90° (full lines) and (d) ϕ_H = -90° (dashed lines).

As observed experimentally, the resonance gradually evolves from a single dip shape (Fig. 6(a)) to a Lorentzian-derivative shape around ϕ_H = 30-37° (b), and finally to a double dip around ϕ_H = 90° (c). Let us focus in particular on the latter curve. To understand its unusual shape, it is useful to explicit how amplitude variations are impacted by the position of the magnetization via magnetoelastic field components, $(b_\theta, b_\phi)\,(\phi_{\rm eq})$ and the magnetic eigenfrequency $\omega_0(\phi_{\rm eq})$

$$\begin{aligned}\Delta\Gamma \propto \Re\left(\Delta P_{\rm mag}\right) &= -\frac{2\pi f M_s}{2}\Im\left(|b_\theta|^2\chi_{11} + |b_\phi|^2\chi_{22} + 2i\chi_{12}|b_\phi b_\theta|\right)\\ &\propto \omega^2\frac{\alpha M_s\left(|b_\theta|^2+|b_\phi|^2\right)\left(\omega^2-\omega_0^2\right) - \gamma B_\alpha\left[\gamma\left(|b_\theta|^2E_{\phi\phi}+|b_\phi|^2E_{\theta\theta}\right)+2\omega|b_\phi b_\theta|M_s\right]}{\left(\omega_0^2-\omega^2\right)^2+\left(\omega\gamma B_\alpha\right)^2}\end{aligned} \tag{10}$$

In these expressions it is assumed that the magnetization lies fully in-plane. E_{ij} are the second derivatives of the total energy with respect to angular coordinates θ, ϕ. Their full expressions, as well as that of B_α, are given in SI section C. What is noteworthy here is that $b_\phi = 0$ and $E_{\phi\phi} \approx 0$ when $\phi_{eq} = \phi_H = 0°$ and is at a minimum when $\phi_{eq} = 0°$ and $\phi_H = \pi/2$. Finally, $B_\alpha \propto \alpha(E_{\phi\phi} + E_{\theta\theta})$, so that SAW amplitude variations are clearly proportional to α, as expected for wave absorption.

Figure 7 shows plots for up and down field-sweeps of the equilibrium angle, the magnetoelastic fields, and the eigenfrequency f_0 when $\phi_H = 90°$. Fig. 7(d) shows that resonance would be expected around 0.9 mT, when the SAW frequency is closest to the eigenfrequency minimum. However, at this precise field $\phi_{eq} = 0$ (Fig. 7(b)), so that $b_\phi(\phi_{eq}) = 0$ (Fig. 7(c)) and $E_{\phi\phi}$ is minimum. From Eq. 10 it follows that in this case a "hole" is carved out of the expected resonance curve, around which two dips form at ± 0.5 mT and ± 1.2 mT. Hence they do *not* correspond to distinct resonance positions, or hysteretic switching steps as could have been expected from data analysis for $\phi_H = 0°$. Indeed, the hysteresis cycle (Fig. 7(b)) shows that the switching step is in fact much higher, around ± 4.6 mT.

We finally briefly comment on amplitude non-reciprocity of $\Delta\Gamma$. As mentioned by other authors,[25] non-reciprocity stems from the competition between the π antisymmetric $\cos(\phi_{\mathrm{eq}})$ term and the $\sin(2\phi_{\mathrm{eq}})$ term in the magneto-elastic field (Eq. 6). It does not come into play when magnetization is strictly parallel or perpendicular to $\boldsymbol{k}$. This was the case for $\phi_H = 0°$ when we had simplified the system by taking $\phi_u = 0°$. A weak non-reciprocity has now appeared for $\phi_H = 0$ and $90°$ when $\phi_u = -6°$ (Fig. 6(e,g)), because this leads to a static equilibrium position of the magnetization that is not rigorously aligned with the SAW wave-vector. At the higher frequency, it becomes very pronounced, a feature reproduced by the hysteretic SAW-FMR model (Fig. 6(d,h)). It stems from the growing weight of the shear strain and rotation terms in the magneto-elastic field (Eq. 6), combined with a tilt of the magnetization away from $0°$ or $90°$ off the SAW wavevector. The shapes of the modeled curves for $\phi_H = 90°$ remain slightly different from experimental ones, due

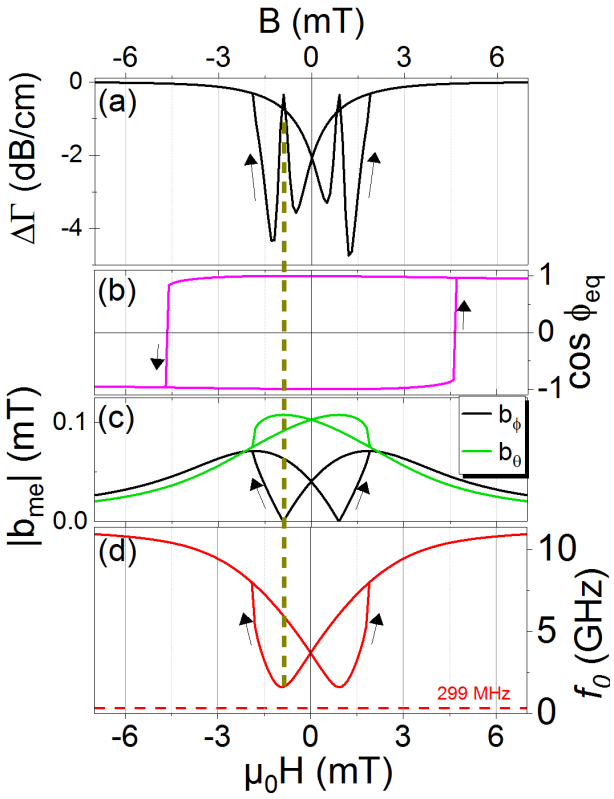

Figure 7: Explanation of the double-dip shape of the amplitude variation curve for $\phi_H = 90°$ (f = 299 MHz, same model curve as in Fig. 6(g)). The panels shown (a) SAW amplitude variations, (b) equilibrium angle, (c) amplitude of the magneto-elastic field components, and (d) eigenfrequency. SAW frequency f=299 MHz is indicated by the horizontal red dashed line. See SI section C and equations within the text for the full analytical expressions of the eigenfrequency and the magneto-elastic fields. The dashed vertical line is a guide for the eyes to follow the position of the eigenfrequency minimum (±0.9 mT).

to the presence of an additional non-hysteretic V-shaped background slope in the data, that is also present in velocity variations curves. This could be due to the presence of an out-of-plane magnetization component, caused by either a slight field misalignment or an out-of-plane anisotropy inducing weak stripes in the sample at low fields. However, our sample characterization setup is not presently sufficient to test these hypotheses further.

4.5 Discussion

While providing a good qualitative description of experimental data, the model discussed in the previous section relies on a strong simplification of the physical system that obviously limits the quantitative match between numerical computations and experiments. We discuss in particular discrepancies on resonance position, depth, and overall curve shape.

As explained above, the position of the resonance is governed by the static magnetization orientation. The latter has been obtained by minimizing a macrospin energy including depinning and uniaxial terms. Whereas the former is likely related to the polycrystalline nature of the layer,[21] the latter can tentatively be attributed to the presence of a Rh gradient across the layer (see SI section A for details on sample growth), and is compatible with the tilted anisotropy axis that appears in the angular dependence of the resonance field (Fig. 4(c)). However it is well-known that hysteresis is a macroscopic phenomenon involving defects and inhomogeneities, with the coercive field potentially smaller than the Stoner-Wohlfarth switching field, $\mu_0 H_{sw}$. As such, a better quantitative agreement with resonance fields over the entire span of field angles would require an independent characterization of the hysteresis, which could not be performed due to the technical constraints mentioned above. The correct prediction of the resonance field also affects the shape of the curve. To illustrate this, let's comment on the case of a field applied along the SAW wavevector. If the magnetization switching occurs before $\mu_0 H_{sw}$, which is the field softening the eigenfrequency, the resonance will not present the rounded minimum of Fig. 6(e), but the sharp minimum experimentally for ϕ_H=0 (Fig. 6(a)).

The SAW resonance *depth* on the other hand is impacted by two factors: the magnetoelastic constant and the overlap of spin and acoustic waves. Our model estimates it correctly for field angles that are close to the SAW wavevector direction, but overestimates amplitude variations as the angle ϕ_H increases. The magnetoelastic constant B_s is the main lever for SAW-driven FMR. The value we have converged to, 5 MJm^{-3}, corresponds to a magnetostriction coefficient[33] $\lambda_s = -\frac{B_s}{3C_{44,\mathrm{iso,FeRh}}} = 22$ ppm ($C_{44,\mathrm{iso,FeRh}}$ being one of the elastic constants of FeRh, see SI section B), a value that is difficult to compare to the experiments of Levetin *et al.*[31] that were performed at high fields. This value however allows to counterbalance the M_s-dependent magneto-rotation term in Eq. 6 and to reproduce the strong non-reciprocity at $f = 889$ MHz for $\phi_H = 90°$ (Fig. 6(d,h)). Secondly, the present model relies on the crude approximation of thickness-averaged dynamic strain and magnetization. A more correct approach would involve calculating the actual overlap of strain and spin waves in the thickness of the sample, at varying field angles.[36] In particular, as the static magnetization is more and more misaligned with the SAW wavevector, the spin wave will tend to localize increasingly at one interface or the other (the so-called Damon-Eschbach mode configuration).

Finally, the description of hysteresis in a macrospin formalism, while convenient, does not take into account the presence of magnetic domains, and how they could affect or be affected by the traveling SAW. Whereas the domain walls themselves are probably too narrow (< 100 nm) to be felt by the SAW ($\lambda > \mu m$), one could imagine the case of an organized domain structure *perpendicular* to the SAW wavevector for which the wavelength would be commensurate with their period. This could induce a measurable attenuation at very particular field angles. However, since our measurement is only sensitive to acoustic waves whose wavevector points perpendicular to the IDTs, only **k**-conserving scattering effects would be detectable in the phase velocity variations.

5 Conclusion

Hysteretic SAW-FMR has been observed experimentally in FeRh and a clear correlation between resonance and coercivity was highlighted. Using a very simple phenomenological macrospin model of hysteresis, the effect has been tracked down to a combination of two phenomena: (i) coercivity of the eigenfrequency whose softening allows for the resonance, (ii) hysteresis of the effective magneto-elastic field. This explains how to reach resonance for both low magnetic fields *and* low SAW frequency, without relying on the presence of a magnetic hard axis. This is a particularly appealing perspective in view of applications. The microscopic origin of hysteresis (domain-wall depinning, uniaxial or biaxial anisotropy, etc.) is not of particular importance here, the only relevant information being the field-history of the static magnetization. The frequency-dependence of the observed features are also a clear illustration of the necessity to take into account the frequency-dependence of the strain components, in particular of the weight of shear strain and rotation terms, even at relatively low frequencies. Looking towards SAW-based applications such as field sensors, resonators, and magnetic delay lines, for which clever solutions have been devised to avoid hysteresis, such a model could be used to harness hysteresis to obtain a large, resonant device response at very moderate magnetic fields.

Acknowledgement

This work has been supported by the French *Agence Nationale de la Recherche* (ACAF ANR-20-CE30-0027 and MAXSAW ANR-20-CE24-0025). We thank D. Hrabovsky (MPBT - *Mesures Physiques à Basses Températures* - Low-Temperature Physical Properties Facility of Sorbonne University) for help with magnetometry experiments. We acknowledge the technical assistance of M. Bernard and M. Vabre (INSP), and thank P. Rovillain and M. Marangolo (INSP) for fruitful discussions on the manuscript.

Supporting Information Available

The Supplementary information contains 5 different sections:

- A: Details on sample fabrication
- B : Details on calculation of acoustic properties
- C : Susceptibility tensor and eigenfrequency
- D: General form of magneto-elastic fields
- E : Extra experimental data

There are also two animated movies showing the full angular dependence of SAW amplitude and phase velocity variations for the two frequencies.

References

(1) Delsing, P. et al. The 2019 surface acoustic waves roadmap. *Journal of Physics D: Applied Physics* **2019**, *52*, 353001.

(2) Ganguly, A. K.; K.L., D.; Webb, D.; Vittoria, C. Magnetoelastic surface waves in a magnetic film–piezoelectric substrate configuration. *Journal of Applied Physics* **1976**, *47*, 2696.

(3) Weiler, M.; Dreher, L.; Heeg, C.; Huebl, H.; Gross, R.; Brandt, M. S.; Goennenwein, S. T. B. Elastically Driven Ferromagnetic Resonance in Nickel Thin Films. *Physical Review Letters* **2011**, *106*, 117601.

(4) Feng, I.; Tachiki, M.; Krischer, C.; Levy, M. Mechanism for the interaction of surface waves with 200-Å nickel films. *Journal of Applied Physics* **1982**, *53*, 177–193.

(5) Rovillain, P.; De Oliveira, R. C.; Marangolo, M.; Duquesne, J.-Y. Nonsymmetric spin pumping in a multiferroic heterostructure. *Physical Review B* **2020**, *102*, 184409.

(6) Hernández-Mínguez, A.; Macià, F.; Hernàndez, J. M.; Herfort, J.; Santos, P. V. Large Nonreciprocal Propagation of Surface Acoustic Waves in Epitaxial Ferromagnetic/Semiconductor Hybrid Structures. *Physical Review Applied* **2020**, *13*, 044018.

(7) Thevenard, L.; Gourdon, C.; Prieur, J. Y.; von Bardeleben, H. J.; Vincent, S.; Becerra, L.; Largeau, L.; Duquesne, J.-Y. Surface-acoustic-wave-driven ferromagnetic resonance in (Ga,Mn)(As,P) epilayers. *Physical Review B* **2014**, *90*, 094401.

(8) Hanna, S. M.; Murphy, G. P. Interactions between magnetostatic and surface acoustic waves in garnet films. *IEEE Transactions on Magnetics* **1988**, *24*, 2814–2816.

(9) Küß, M.; Glamsch, S.; Kunz, Y.; Hörner, A.; Weiler, M.; Albrecht, M. Giant Surface Acoustic Wave Nonreciprocity with Low Magnetoacoustic Insertion Loss in CoFeB/Ru/CoFeB Synthetic Antiferromagnets. *ACS Applied Electronic Materials* **2023**, *5*, 5103–5110.

(10) Lyons, T. P.; Puebla, J.; Yamamoto, K.; Deacon, R. S.; Hwang, Y.; Ishibashi, K.; Maekawa, S.; Otani, Y. Acoustically Driven Magnon-Phonon Coupling in a Layered Antiferromagnet. *Physical Review Letters* **2023**, *131*, 196701.

(11) Küß, M.; Hassan, M.; Kunz, Y.; Hörner, A.; Weiler, M.; Albrecht, M. Nonreciprocal magnetoacoustic waves in synthetic antiferromagnets with Dzyaloshinskii-Moriya interaction. *Physical Review B* **2023**, *107*, 024424.

(12) Mazzamurro, A.; Dusch, Y.; Pernod, P.; Bou Matar, O.; Addad, A.; Talbi, A.; Tiercelin, N. Giant Magnetoelastic Coupling in a Love Acoustic Waveguide Based on Nanostructured Film on ST-Cut Quartz. *Physical Review Applied* **2020**, *13*, 044001.

(13) Polewczyk, V.; Dumesnil, K.; Lacour, D.; Moutaouekkil, M.; Mjahed, H.; Tiercelin, N.; Petit Watelot, S.; Mishra, H.; Dusch, Y.; Hage-Ali, S.; Elmazria, O.; Montaigne, F.; Talbi, A.; Bou Matar, O.; Hehn, M. Unipolar and Bipolar High-Magnetic-Field Sensors Based on Surface Acoustic Wave Resonators. *Physical Review Applied* **2017**, *8*, 024001.

(14) Hu, W.; Huang, M.; Xie, H.; Zhang, H.; Bai, F. Self-Biased Magnetic Field Sensors Based on Surface Acoustic Waves through Angle-Dependent Magnetoacoustic Coupling. *Physical Review Applied* **2023**, *19*, 014010.

(15) Kittmann, A.; Müller, C.; Durdaut, P.; Thormählen, L.; Schell, V.; Niekiel, F.; Lofink, F.; Meyners, D.; Knöchel, R.; Höft, M.; McCord, J.; Quandt, E. Sensitivity and noise analysis of SAW magnetic field sensors with varied magnetostrictive layer thicknesses. *Sensors and Actuators A: Physical* **2020**, *311*, 111998.

(16) Li, B.; Al, H.; Kosel, J. *Modeling and Measurement Methods for Acoustic Waves and for Acoustic Microdevices*; InTech, 2013.

(17) Yang, Y.; Mengue, P.; Mishra, H.; Floer, C.; Hage-Ali, S.; Petit-Watelot, S.; Lacour, D.; Hehn, M.; Han, T.; Elmazria, O. Wireless Multifunctional Surface Acoustic Wave Sensor for Magnetic Field and Temperature Monitoring. *Advanced Materials Technologies* **2022**, *7*, 2100860.

(18) Aguilera, J. D.; Loriente, R.; Soria, L.; Begue, A.; Ranchal, R.; Gràcia, I.; Vallejos, S.; Hernando, A.; Marín, P.; de la Presa, P.; Matatagui, D. Anomalies in the magnetostrictive modulation of love surface acoustic waves. *AIP Advances* **2024**, *14*, 025208.

(19) Kuszewski, P.; Camara, I. S.; Biarrotte, N.; Becerra, L.; von Bardeleben, J.; Savero Torres, W.; Lemaître, A.; Gourdon, C.; Duquesne, J.-Y.; Thevenard, L. Resonant magnetoacoustic switching: influence of Rayleigh wave frequency and wavevector. *Journal of Physics: Condensed Matter* **2018**, *30*, 244003.

(20) Ourdani, D.; Castellano, A.; Vythelingum, A. K.; Arregi, J. A.; Uhlíř, V.; Perrin, B.; Belmeguenai, M.; Roussigné, Y.; Gourdon, C.; Verstraete, M. J.; Thevenard, L. Experimental determination of the temperature- and phase-dependent elastic constants of FeRh. *Physical Review B* **2024**, *110*, 014427.

(21) Ba, D. N.; Olivetti, G.; Tremblais, T.; Boventer, I.; Vidal, F.; Duvauchelle, J.-E.; Gourdon, C.; Thevenard, L. Origin of low-field microwave absorption in metallic magnetic films evidenced in FeRh/Ta/GaAs. *Physical Review B* **2025**, *111*, 014426.

(22) Hepburn, C. Dynamic interplay between the magnetization and surface acoustic waves in magnetostrictive Fe1-xGax thin films. Ph.D. thesis, 2017.

(23) Hatanaka, D.; Asano, M.; Okamoto, H.; Kunihashi, Y.; Sanada, H.; Yamaguchi, H. On-Chip Coherent Transduction between Magnons and Acoustic Phonons in Cavity Magnomechanics. *Physical Review Applied* **2022**, *17*, 034024.

(24) Mancini, E.; Pressacco, F.; Haertinger, M.; Fullerton, E. E.; Suzuki, T.; Woltersdorf, G.; Back, C. H. Magnetic phase transition in iron–rhodium thin films probed by ferromagnetic resonance. *Journal of Physics D: Applied Physics* **2013**, *46*, 245302.

(25) Hernández-Mínguez, A.; Macià, F.; Hernàndez, J. M.; Tejada, J.; Santos, P. V. Phonon-induced quantum magnetic deflagration in. *Journal of Magnetism and Magnetic Materials* **2008**, *320*, 1457–1463.

(26) Hwang, Y.; Puebla, J.; Kondou, K.; Gonzalez-Ballestero, C.; Isshiki, H.; Muñoz, C. S.; Liao, L.; Chen, F.; Luo, W.; Maekawa, S.; Otani, Y. Strongly Coupled Spin Waves and Surface Acoustic Waves at Room Temperature. *Physical Review Letters* **2024**, *132*, 56704.

(27) Rovillain, P.; Duquesne, J.-y.; Christienne, L.; Eddrief, M.; Pini, M. G.; Rettori, A.; Tacchi, S.; Marangolo, M. Impact of Spin-Wave Dispersion on Surface-Acoustic-Wave Velocity. *Physical Review Applied* **2022**, *18*, 064043.

(28) Hwang, Y.; Puebla, J.; Xu, M.; Lagarrigue, A.; Kondou, K.; Otani, Y. Enhancement of acoustic spin pumping by acoustic distributed Bragg reflector cavity. *Applied Physics Letters* **2020**, *116*, 252404.

(29) Royer, D.; Chenu, C. Experimental and theoretical waveforms of Rayleigh waves generated by a thermoelastic laser line source. *Ultrasonics* **2000**, *38*, 891–895.

(30) Ibarra, M. R.; Algarabel, P. A. Giant volume magnetostriction in the FeRh alloy. *Physical Review B* **1994**, *50*, 4196–4199.

(31) Levitin, R.; Ponomarev, B. Magnetostriction of the Metamagnetic Iron-rhodium Alloy. *Soviet Journal of Experimental and Theoretical Physics* **1966**, *23*, 984.

(32) Wu, H.; Liu, Q.; Gao, R.; Mi, S.; Jia, L.; Wang, J.; Liu, H.; Zhang, S.; Wei, J.; Wang, X.; Han, G.; Wang, J. Acoustic Wave-Induced FeRh Magnetic Phase Transition and Its Application in Antiferromagnetic Pattern Writing and Erasing. *ACS Nano* **2024**, *18*, 12134–12145.

(33) du Tremolet de la Lacheisserie, E. *Magnetostriction theory and applications of magnetoelasticity*; CRC Press, 1993.

(34) Maekawa, S.; Tachiki, M. Surface acoustic attenuation due to surface spin wave in ferro- and antiferromagnets. *AIP Conference Proceedings* **1976**, *29*, 542–543.

(35) Yamamoto, K.; Maekawa, S. Magnetostatic Field Induced by Mechanical Deformations. *Annalen der Physik* **2024**, *536*, 1–11.

(36) Yamamoto, K.; Xu, M.; Puebla, J.; Otani, Y.; Maekawa, S. Interaction between surface acoustic waves and spin waves in a ferromagnetic thin film. *Journal of Magnetism and Magnetic Materials* **2022**, *545*, 168672.